

Article

# Gulf Stream Effects on Sea Level Oscillations: Enhancing Performance of a Coastal and Estuarine Model Nested into Global Model through Modified Boundary Conditions

Md Ahsan Habib \* and Gary A. Zarillo

Department of Ocean Engineering and Marine Sciences, Florida Institute of Technology, 150 W University Blvd, Melbourne, FL 32901, USA; zarillo@fit.edu

\* Correspondence: mhabib2014@my.fit.edu

**Abstract:** This study investigates the effects of the gulf stream (GS) on sea-level oscillations across various time scales and assesses the performance of a coastal and estuarine model nested within a global model in simulating these variations. It aims to improve boundary conditions to simulate sea-level oscillations more accurately by considering the influence of GS flow. An inverse correlation is observed between observed sea-level oscillation and GS flow, which becomes more pronounced over longer time scales. Using Delft3D, a high-resolution coastal and estuarine model is developed to simulate circulation dynamics in the central Indian River Lagoon (IRL), FL, and adjacent coastal areas on the Florida east coast. The model is nested into the HYCOM (Hybrid Coordinate Ocean Model), and meteorological forcings are derived from the NARR (North American Regional Reanalysis) model. The model demonstrates satisfactory performance across key parameters, including tide, salinity, water temperature, and currents. However, there remains a noticeable difference between the modeled and observed data. To address this, the model is executed with modified flow boundary conditions at eastern boundary nodes, integrating HYCOM tide, and observing low-frequency sea-level variations. The implementation of the new boundary conditions results in an improved simulation of sea-level oscillations. This study presents the conceptual framework and detailed methodologies employed in the creation of a high-resolution model tailored for estuarine and coastal areas nested into global models capable of satisfactorily simulating sea-level oscillations even when the global model does not represent GS effects.

**Keywords:** Delft3D; coastal and estuarine model; sea-level oscillation; gulf stream; hydrodynamic model; nested model; Indian River Lagoon; HYCOM



**Citation:** Habib, M.A.; Zarillo, G.A. Gulf Stream Effects on Sea Level Oscillations: Enhancing Performance of a Coastal and Estuarine Model Nested into Global Model through Modified Boundary Conditions. *J. Mar. Sci. Eng.* **2024**, *12*, 775. <https://doi.org/10.3390/jmse12050775>

Academic Editor: Abdellatif Ouahsine

Received: 19 March 2024

Revised: 19 April 2024

Accepted: 28 April 2024

Published: 6 May 2024



**Copyright:** © 2024 by the authors. Licensee MDPI, Basel, Switzerland. This article is an open access article distributed under the terms and conditions of the Creative Commons Attribution (CC BY) license (<https://creativecommons.org/licenses/by/4.0/>).

## 1. Introduction

Numerical simulation of estuarine and coastal hydrodynamics yields an understanding of critical processes and predicts water movement and variations in water properties, crucial in marine system research. Thus, a combination of numerical simulation and field data offers an in-depth understanding of coastal and estuarine processes, providing the basis for studying morphology, waves, sediment transport, and water quality. In estuary and coastal systems, the predominant forces comprise tides, low-frequency sea-level oscillations, freshwater discharge, waves, storm surges, and meteorological forcings.

The widespread application of high-resolution coastal modeling has become integral to coastal management systems. Global models, with their low resolution, cannot capture phenomena demanding finer spatial resolution. Hence, nesting a high-resolution coastal model within global models (e.g., HYCOM) proves effective in simulating coastal hydrodynamics. The construction of models, with structured grid, and nesting them into global models offers a practical solution to addressing a broad spectrum of spatial and temporal variation in motions [1–4]. The technique entails allocating data from low-resolution, large-scale models to a high-resolution model, which focuses on a more localized area.

Implementing open boundary forcings in a numerical model is crucial, as they directly influence the accuracy of simulation outcomes. Coastal circulation dynamics differ significantly from those in the deep ocean due to various factors, such as shallowness, tidal effects, nearby coastlines, and freshwater discharges [5]. In coastal areas, bottom-drag forces are more influential, flow convergence and divergence are more prevalent, and horizontal density gradients lead to specific phenomena like surges and buoyancy-driven flows. To minimize computational workload, the model domain is tailored to the specific area of focus. Open boundary forcings are employed to incorporate the influence of areas beyond the modeled domain that are not directly simulated.

The gulf stream (GS), the upper branch of the Atlantic Meridional Overturning Circulation (AMOC), is a powerful ocean current in the North Atlantic Ocean. It tracks along the east coast of the USA before turning offshore at Cape Hatteras to form the North Atlantic Current and transport heat to high latitudes (Figure 1a). The GS plays a crucial role in influencing sea-level variations along the east coast. A direct correlation exists between coastal ocean sea-level oscillations and variations in GS flow [6]. Over the longer period, the rising sea levels observed along the east coast in recent years have been correlated with the deceleration of the GS [6].

When a hurricane follows the GS, even without making significant landfall, coastal areas experience sea-level rise and flooding [7]. This phenomenon was evident during hurricanes Matthew (2016) and Dorian (2019), both of which tracked along the GS. Despite not making substantial landfalls, both hurricanes weakened the GS flow by approximately 50%. As a result, there was a rise in sea levels and a surge in flooding along coastal areas in the days and weeks following these storms.

Given the significant impact of the GS on coastal sea levels, it is crucial to integrate its effects into boundary conditions. Inadequate representation of the GS in flow boundary conditions can lead to an underestimation of sea-level oscillations in coastal regions. Global models, such as HYCOM, often fall short of accurately representing the GS effect [8]. When high-resolution coastal and estuarine models are nested within the global model HYCOM, it can result in underperformance in simulating sea-level oscillations. Accurate simulation of low-frequency sea-level oscillations is of paramount importance, as underestimating sea-level rise could hinder effective coastal resilience planning. Therefore, improving the representation of the GS's effects in boundary conditions is essential for better forecasting and planning for coastal communities.

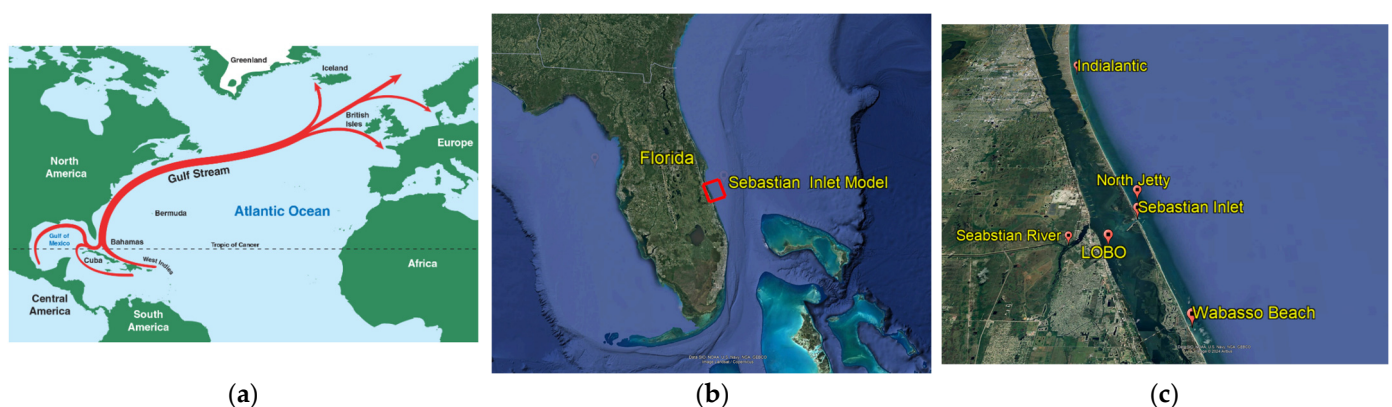


**Figure 1.** (a) Gulf Stream flow path [9]. Model Region: (b) modeling area (red rectangular box) [10]; (c) focused area of interest (Sebastian Inlet) [10].

## 2. Methods

A high-resolution numerical model has been created utilizing Delft3D, which is an open-source, 3-D modeling system based on finite difference methods [11]. This model illustrates the central Indian River Lagoon (IRL) from Wabasso to Indialantic, along with the adjacent coastal region, with a particular emphasis on the Sebastian Inlet.

### 2.1. Study Area

The Indian River Lagoon (IRL), located along the east coast of Florida (see Figure 1b,c), stretches approximately 255 km from Ponce de Leon Inlet to Jupiter Inlet. It encompasses four coastal counties and is connected to the Atlantic Ocean through five narrow inlets: Ponce de Leon, Sebastian, Fort Pierce, St. Lucie, and Jupiter Inlets. Sebastian Inlet holds a central position within the lagoon. The IRL receives freshwater inputs from precipitation, groundwater seepage, and surface water runoff originating from creeks and streams.

The IRL can be divided into three distinct segments: the northern segment from Mosquito Lagoon to Sebastian Inlet, the central segment from Sebastian Inlet to Fort Pierce Inlet, and the southern segment from Fort Pierce Inlet to Jupiter Inlet, including the St. Lucie estuary. The hydrodynamic characteristics of the lagoon are influenced by several factors, including tidal forcing, low-frequency coastal sea-level variations, freshwater inflows, complex bathymetry and coastline geometry, and meteorological forcing. The specific dominant factors vary across the different segments.

In the northern segment, tidal effects are minimal, resulting in small water level changes and weak currents, except during periods of high winds. Salinity in this segment exhibits a broad range and strongly depends on local precipitation and freshwater runoff. Low-frequency water level variations play a more significant role than tidal forcings, making coastal sea level a key factor in this segment [12,13].

The central segment is strongly influenced by tidal dynamics from Sebastian and Fort Pierce Inlets, as well as freshwater runoff from the Sebastian River. Salinity levels in this segment are typically high due to limited freshwater runoff and significant exchanges with the ocean through the inlets.

### 2.2. Model Grid

A numerical model was developed for the central IRL, utilizing Delft3D [9]. The model employed a curvilinear orthogonal computational grid, with grid size varying from 14 m in the IRL and inlet to 475 m in the coastal region (Figure 2) and is composed of 5 vertical layers. The grid illustrates the central Indian River Lagoon (IRL) from Wabasso to Indialantic, along with the adjacent coastal region (Figure 1a,b).

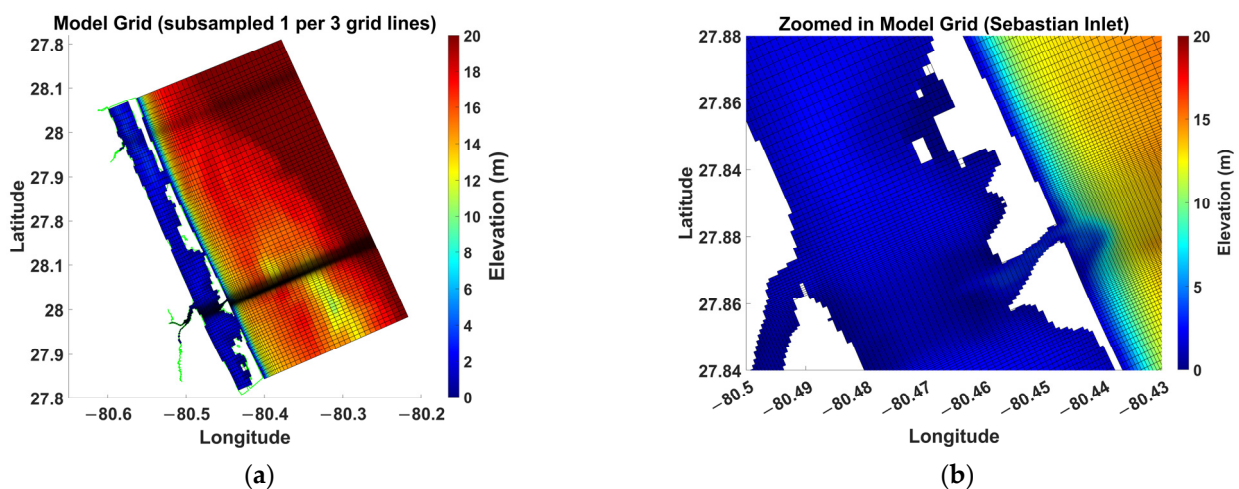


**Figure 2.** Grid: (a) full model domain (every third grid line) and topography; (b) zoomed-in mesh near Sebastian Inlet.

### 2.3. Data Sources

The data was gathered from multiple sources, as outlined in Table 1.

**Table 1.** Model data and their origins, web address, and resolution.

Parameters	Source	Web Address	Resolution
Topography	NCEI NOAA	<a href="https://www.ncei.noaa.gov">https://www.ncei.noaa.gov</a> (retrieved on 13 November 2021)	0.005556 <sup>0</sup>
sea surface elevation, salinity, and water temperature	HYCOM	<a href="https://www.hycom.org/data/gomb0pt04/gom-reanalysis">https://www.hycom.org/data/gomb0pt04/gom-reanalysis</a> (retrieved on 19 April 2022)	1/25 <sup>0</sup>
Gulf stream flow	AOML NOAA	<a href="https://www.aoml.noaa.gov/phod/floridacurrent/data_access.php">https://www.aoml.noaa.gov/phod/floridacurrent/data_access.php</a> (retrieved on 14 December 2023)	Time series
Water level and ADCP	Florida Tech	<a href="https://research.fit.edu/wave-data/real-time-data/">https://research.fit.edu/wave-data/real-time-data/</a> (retrieved on 7 June 2020)	Time series
u and v component of wind velocity, rel. humidity, evaporation, and heat flux	NARR	<a href="https://rda.ucar.edu/">https://rda.ucar.edu/</a> (retrieved on 11 April 2022)	20 miles
Salinity, water temperature	HBOI-LOBO	<a href="http://fau-hboi.loboviz.com/loboviz/">http://fau-hboi.loboviz.com/loboviz/</a> (retrieved on 25 February 2020)	timeseries
River discharge	SJRWMD	<a href="https://www.sjrwmd.com/data/">https://www.sjrwmd.com/data/</a> (retrieved on 20 March 2019)	timeseries

### 2.4. Model Setup

This model's configuration closely aligns with the approach outlined in [8]. The description of Delft3D, topographic data collection, vertical layer distribution, bottom roughness setup, flow, and transport boundary conditions can be found in the study in [8]. Topographic data were obtained from the NOAA coastal digital elevation model [14] to create the model's topography (Figure 3). Figure 4a illustrates all 11 nodes for flow and transport boundary forcings. Water level data were chosen as flow boundary forcings (Figure 4b). Transport boundary conditions, consisting of salinity and water temperature, are presented in Figure 5. The surface elevation, water temperature, and salinity data are obtained from HYCOM [15] and applied to the model as open boundary conditions. The surface elevation data derived from HYCOM includes five major tidal constituents (M2, S2, O1, K1, and N2), eliminating the need for additional tidal inputs into the model. Meteorological forcings, including the u and v components of wind, air temperature, relative humidity, and evaporation (Figure 6), are derived from the NARR model [16] and applied to the Delft3D model as surface boundary conditions. The river discharges (bottom panel in Figure 6a) data (daily mean) were collected from SJRWMD [17] for Sebastian River gauges (see location in Figure 1c). The meteorological forcings were uniformly applied over the model domain. The model incorporates five vertical sigma layers over the entire model domain. It employs the k-epsilon turbulence formulation to simulate vertical turbulent eddy viscosity and eddy diffusivity. The numerical scheme utilized is the alternating direction implicit (ADI) scheme [18–20]. The bottom roughness was defined under the Chezy formulation, which is widely used in open channel flow calculations in which the Chezy coefficient relates roughness elements and Reynolds number to flow velocity. The absolute flux model (based on the total solar radiation) was applied for heat flux formulation. The absolute flux model [21] involves prescribing the incoming (short-wave) solar radiation while computing the net atmospheric (long-wave) radiation and the heat losses resulting from evaporation, outgoing radiation, and convection.

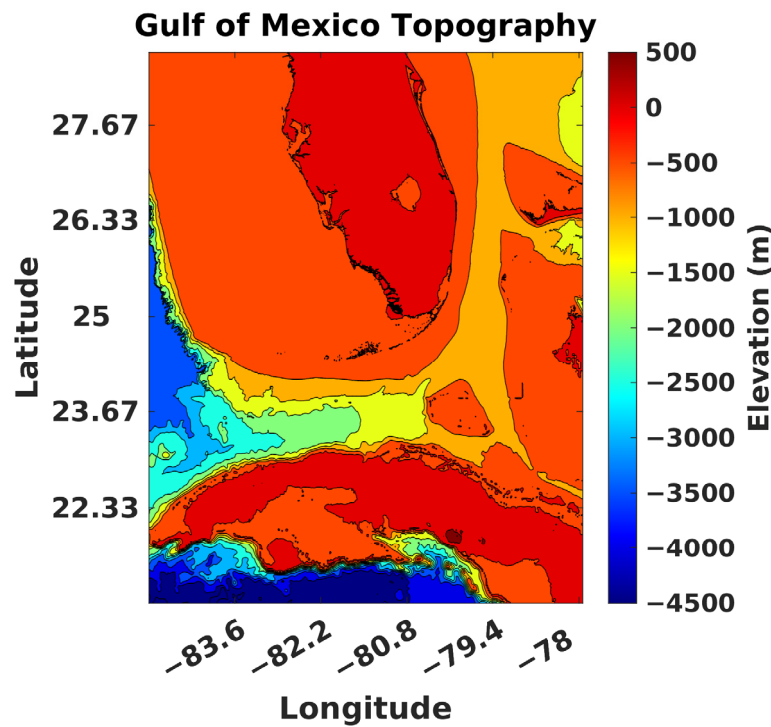


Figure 3. Bathymetry data obtained from the NOAA [14].

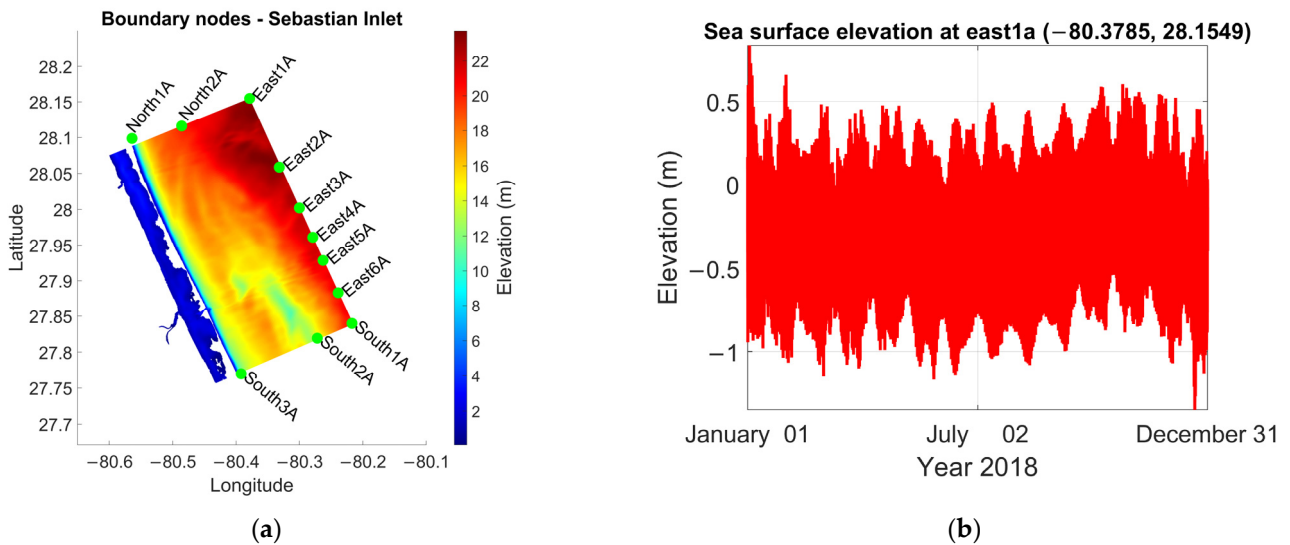


Figure 4. (a) Boundary nodes for open boundary conditions; (b) flow boundary condition at East1A node (labeled as East1A in (a)).

### 2.5. Model Adjustments and Calibration

Model calibration followed a similar approach to that outlined in [8]. A two-year calibration simulation, spanning from 2018 to 2019, was undertaken to refine the model’s accuracy. A sequence of numerical experiments was carried out to evaluate the influence of these parameters in the model. In the CONTROL experiments, the model consisted of five sigma layers, featured a Chezy parameter of 55, and was driven by spatially varying 2-D winds. Furthermore, three experiments were carried out, wherein (1) the bottom friction parameter was varied to 55, 80, and 100, (2) the number of vertical layers was increased to 10, and (3) spatially uniform 1-D winds were applied from a designated location near Sebastian Inlet beyond the harbor. All other parameters remained constant throughout these experiments. The study conducted by [8] provides comprehensive details

on the methods employed, statistical analyses conducted, and plots generated for these calibration experiments.

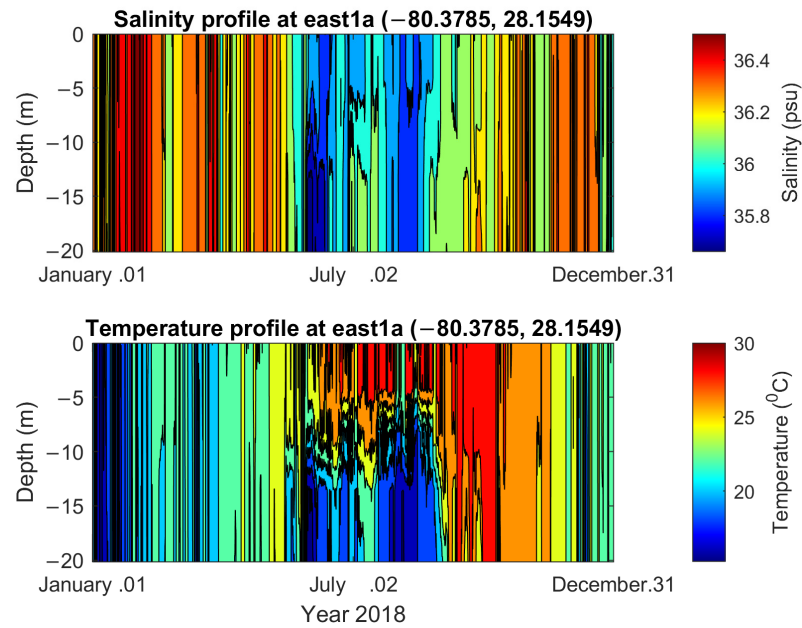


Figure 5. Depth profile of salinity (upper section) and water temperature (lower section) at the East1A node.

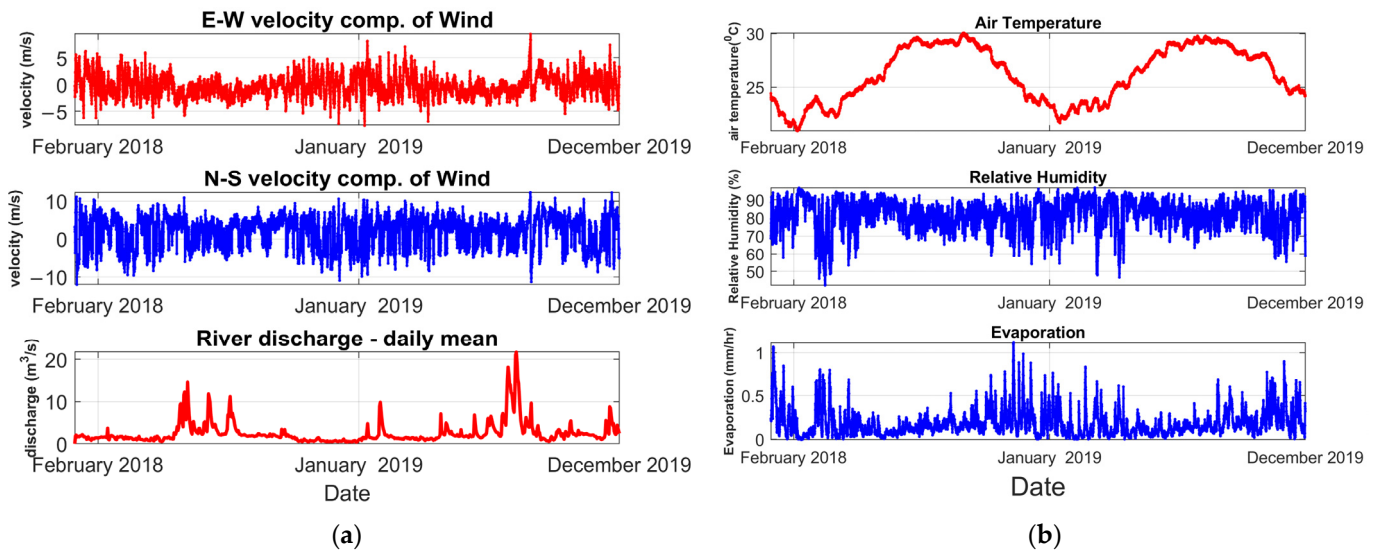


Figure 6. (a) Surface wind velocity components ((upper and middle panels)) and freshwater discharge (bottom panel) for the year 2018–2019; (b) relative humidity (upper section), evaporation (central section), and air temperature (lower section) for the year 2018–2019.

### 3. Model Performance and Skills

The following segment presents a sequence of evaluations between the simulation outcomes and accessible observed data to showcase the model’s effectiveness and competence. Quantitative metrics are also calculated to assess the disparities between the simulated results and observations. All model outcomes presented here are derived from the control setup.

### 3.1. Salinity and Water Temperature

The salinity and water temperature obtained from the simulation were compared with observed data at the LOBO station [22]. The simulated salinity captured the overall trends of the salinity time series; however, it did not simulate the variations in the time series (Figure 7a). The primary factor contributing to this discrepancy is the unavailability of data from all sources of freshwater discharges. In this model, only discharge data from the Sebastian River was utilized, as it was the sole available source. The water temperature time series comparison at the LOBO station showed a good match between the observed and model output, with only slight deviations at a few time points (Figure 7b). The water temperature time series exhibited a similar trend for both the measured and simulated data, although, like salinity, it did not capture a few of the lowest points in the time series.

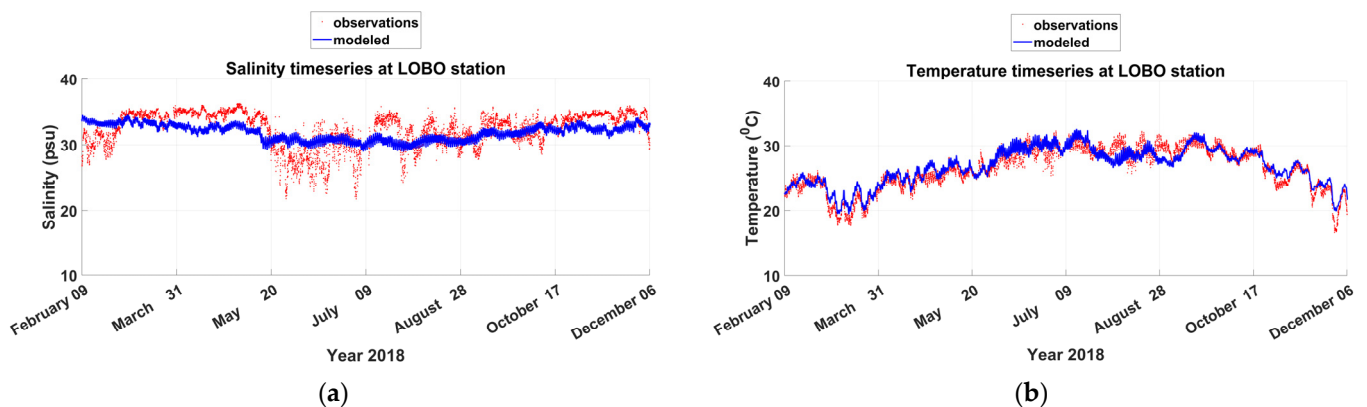


**Figure 7.** (a) Modeled (blue line) and observed salinity (red dots) at LOBO station (see location in Figure 1c); (b) modeled (blue line) and observed (red dots) water temperature at LOBO station.

### 3.2. Currents

A transect has been drawn along the Indian River Lagoon (IRL) from Wabasso in the south to Indialantic in the north (see location in Figure 1c). Figure 8 displays the E-W and N-S horizontal velocity component profiles along this transect. These profiles provide insights into the spatial variations of the velocity profile within the central IRL. Near the Sebastian Inlet region, both the E-W and N-S velocity components exhibit stronger currents. This is likely due to the influence of tidal dynamics and the presence of nearby inlets, which can enhance water flow and create localized areas of increased current intensity.

On the other hand, the northern section of the IRL experiences weaker currents compared to the region near Sebastian Inlet. The weaker current in this area can be attributed to a range of factors, including geomorphological constraints and random factors that affect the flow dynamics within the lagoon. It is noteworthy that the N-S velocity component is approximately two times stronger than the E-W component. This indicates that the dominant flow direction within the lagoon is predominantly in the N-S direction. The stronger N-S component could be influenced by the geometrical configuration of the lagoon and the prevailing tidal and wind patterns in the region. Overall, the velocity component profiles highlight the spatial variability in water currents along the IRL, with stronger currents near the Sebastian Inlet and a weaker flow in the northern section of the lagoon. During flood tide, seawater is pushed into the estuary, flowing southward in the southern section of the IRL and northward in the northern part. Conversely, during ebb tide, water is pushed back into the ocean. Throughout both tidal cycles, the northern IRL experiences less influence from the tides due to its relatively greater distance from the inlet.

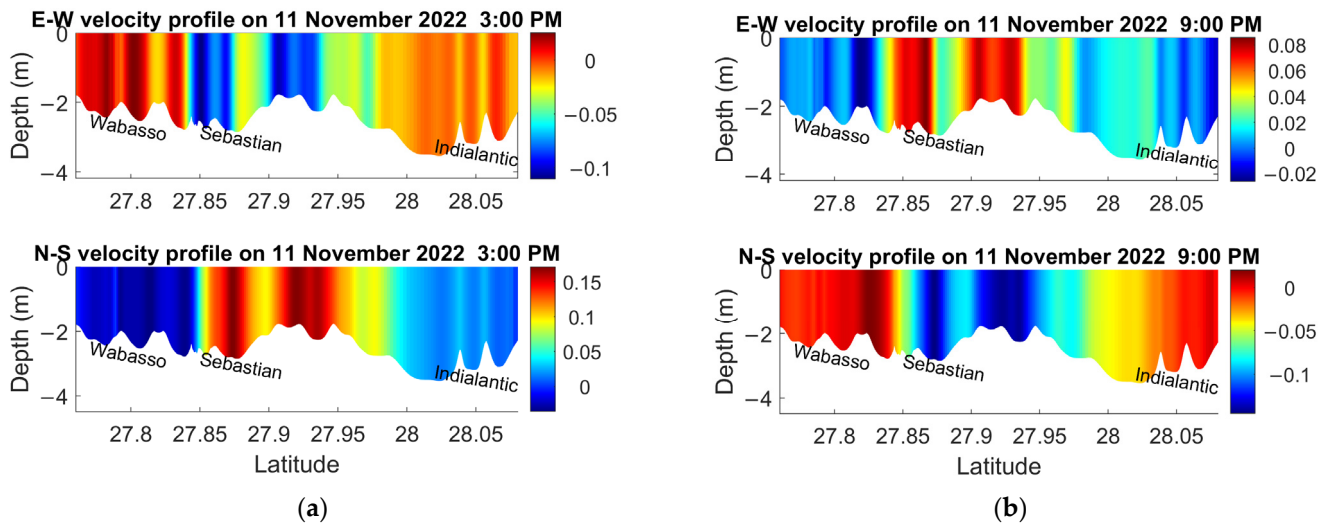


**Figure 8.** (a) Depth profile of horizontal velocity components in the latitude direction, from Wabasso beach in the South to Indialantic beach in the north (see location in Figure 1c), during flood tide; (b) depth profile of horizontal velocity components in the latitude direction, from Wabasso in the south to Indialantic in the north, during ebb tide.

3.3. ADCP Data

The top panels in Figure 9a and Figure 9b display the E-W and N-S velocity component profiles, respectively, obtained from the acoustic doppler current profiler (ADCP) deployed at the Florida Tech wave monitoring station between 9 November 2022, and 22 November 2022 [23]. The ADCP data presents an E-W velocity predominantly ranging from  $-0.3$  to  $0.4$  m/s and an N-S velocity ranging from  $-0.4$  m/s to  $0.3$  m/s. The bottom panels in Figure 9a,b present the modeled velocity profiles at a grid cell near the Florida Tech weather station. The modeled velocity ranges from  $-0.2$  m/s to  $0.2$  m/s. The model does not reproduce the high-frequency variations observed in ADCP data, and there is no significant correlation between the modeled results and the observed data.

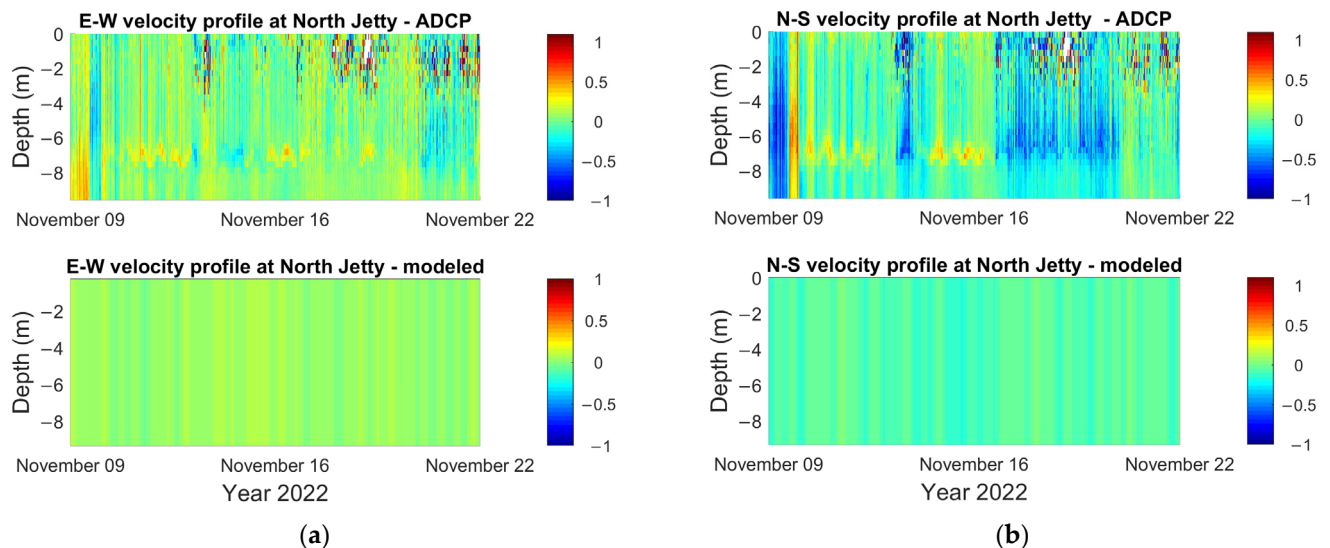


**Figure 9.** (a) Depth profile of the E-W component of horizontal velocity for ADCP (top panel) and modeled (bottom panel) at North Jetty station; (b) similar plot for depth profile of the N-S component of horizontal velocity at the same station.

Several factors may account for the disparity between the velocity profiles. Firstly, large grid cells may lead to the smoothing out of fine-scale features and high-frequency variations present in the measurements. Additionally, the model assumes uniform bottom friction, which may not accurately represent the complex frictional characteristics of the actual system, further contributing to the differences between the velocity profiles. Further calibration experiments could be performed to improve the modeled results.

### 3.4. Water Level

The modeled water level was compared with measurements at North Jetty station [23], and good agreement was observed with a small difference between them (upper panel in Figure 10a). The difference between observed and modeled water level data (bottom panel in Figure 10a) is further investigated in the following sections. The correlation comparison in Figure 10b shows that the correlation between water levels is 96%.

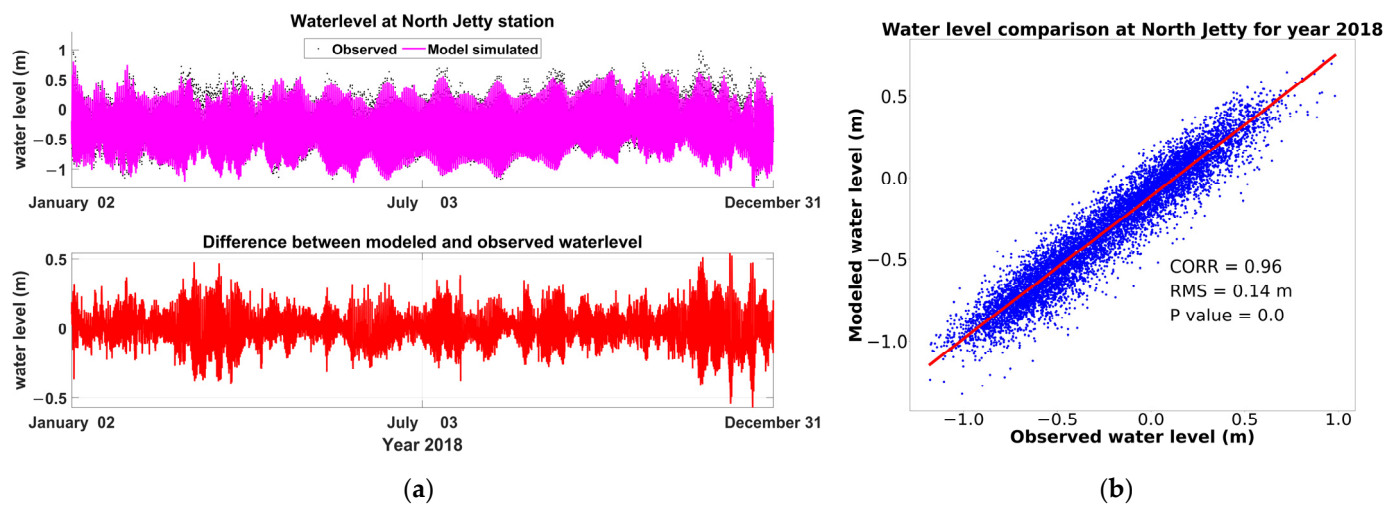


**Figure 10.** (a) Simulated (magenta colored line) and measured (black dots) water level at North Jetty station for year 2018 (**top panel**), differences between modeled and observed data (**bottom panel**); (b) scatter plot for water levels for observed and modeled data at North Jetty for year 2018.

### 3.5. Tide

A comparison between observed and modeled tides, extracted using the `t_tide` MATLAB toolbox [24], is depicted in Figure 11a. The comparison illustrates that the model-simulated tide aligns well with the observed tide. The water level differences between simulated and observed values span between  $-0.5$  m and  $0.5$  m (bottom panel in Figure 10a), while the differences between both tides range from  $-0.1$  m to  $0.1$  m (bottom panel in Figure 11a). These comparisons underscore that the disparity between observed and modeled data is primarily attributed to nontidal forcings. Therefore, a detailed examination of the comparison between nontidal forcings is carried out in the following sections.

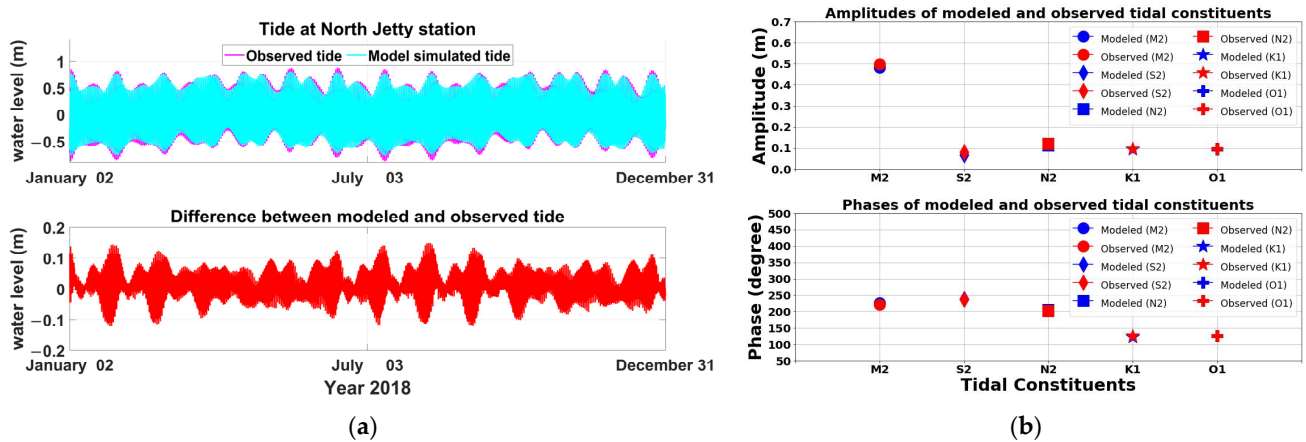


Figure 11. (a) Observed (magenta colored line) and simulated (cyan colored line) tide at North Jetty station (top panel), and differences between modeled and observed tide (bottom panel); (b) modeled and observed tidal constituents (M2, S2, N2, K1, and O1) at North Jetty station.

#### 4. Effects of Gulf Stream

##### 4.1. Nontidal Forcings

A Lanczos filter, with a cutoff period of 12.4 h, was employed to remove the M2 tidal component and extract nontidal flow from both observations and simulated water level data. Additionally, nontidal forcings were extracted from the HYCOM node closest to the North Jetty station. The comparison of the extracted nontidal forcings (Figure 12a) reveals a significant discrepancy between observations (red line) and modeled data (blue line). However, the modeled low-frequency variations closely align with those of the HYCOM (green line). Further clarification of these differences is presented in Figure 12b, where the disparities between modeled and HYCOM low-frequency variations align closely to 0, while the differences between modeled and observed data range from  $-0.2$  m to  $0.5$  m. These comparisons establish that the model’s inability to simulate low-frequency oscillations stems from the applied boundary conditions. The HYCOM surface elevation data used as flow boundary forcings lacks representation of low-frequency sea-level oscillations. This deficiency is reflected in Figures 10 and 12, accounting for the discrepancy between simulated and observed water levels.

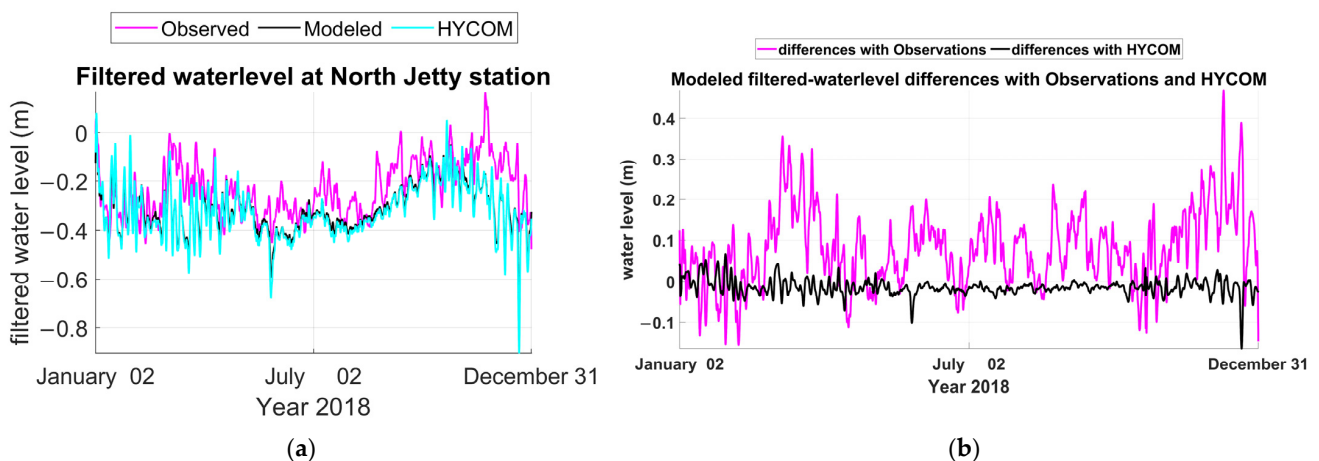
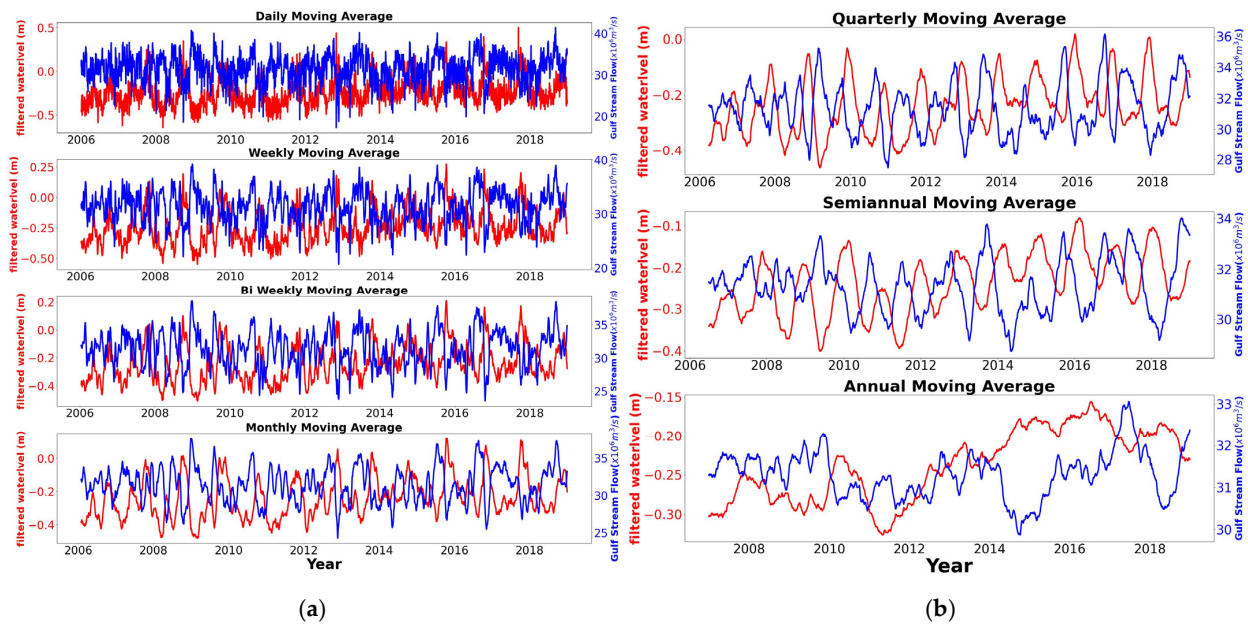


Figure 12. (a) Nontidal component of water level for measured (magenta line), simulated (black colored line), and HYCOM data (cyan colored line) at North Jetty station; (b) differences between simulated and measured residuals (magenta colored line) and differences between simulated and HYCOM residuals (black colored line).

#### 4.2. Gulf Stream Flow

The GS plays a significant role in sea-level variations along the east coast [6]. Changes in the flow rate of the GS directly impact the rise and fall of sea level. By examining the relationship between GS flow and the modeled and observed water level, a better understanding can be gained regarding the factors contributing to the amplitude disparity (bottom panel in Figure 10a) observed in the simulations.

The effects of the GS current on sea-level variations are examined in this study. In Figure 13a, a comparison is presented between the observed low-frequency variations at the north jetty station and the GS flow on different time scales, including daily, weekly, biweekly, and monthly moving averages. In Figure 13b, a similar comparison is made on quarterly, semiannual, and annual time scales. The GS flow was collected from the NOAA Atlantic Oceanographic and Meteorological Laboratory [25]. Both the GS flow and low-frequency sea-level variations are processed using moving averages for each respective time scale. The resulting moving average comparisons between the observations and the GS flow are plotted in Figure 13. The inverse correlation between the nontidal forcings at the water level and the GS flow is evident in the figures. The rise and fall of the sea level correspond to the decrease and increase in the flow rate of the GS. This correlation becomes more apparent when observing over longer time scales. These comparisons provide valuable insights into the relationship between the GS flow and the water level variations, highlighting the influence of the GS on the sea-level oscillations. The findings demonstrate that changes in the GS flow have a direct impact on the observed and modeled water levels, with a stronger correlation observed on longer time scales.



**Figure 13.** Gulf stream effects: (a) observed filtered-water level (left axis) at the north jetty and Florida current transport data (right axis) on different time scales: daily (1st panel from top), weekly (2nd panel), biweekly (3rd panel), and monthly (bottom panel) moving averages. Moving averages for each respective time scale are calculated for both GS flow and filtered-water level; (b) observed filtered-water level (left axis) at the North Jetty and Florida current transport data (right axis) on various time scales: quarterly (top panel from top), semiannual (middle panel), and annual (bottom panel) moving averages.

Table 2 displays the Pearson correlation coefficient and corresponding statistical significance  $p$ -values, illustrating the comparison between the observed sea-level and GS flow across various time scales. The correlation tends to improve with longer time scales, peaking at the quarterly moving average. However, beyond this point, the correlation

diminishes, approaching zero on an annual scale. Additionally, GS flow is lagged by 1, 2, 3, weeks, and 1 month to calculate the Pearson correlation. Analysis reveals that as the lag time increases, the correlation also increases, reaching optimal values at the 3-week lag steps before declining. This analysis suggests a direct relationship between the rise and fall of sea level and the corresponding decrease and increase in GS flow, with the maximum correlation observed at the quarterly time scale and a lag of 3 weeks between GS flow and sea level.

**Table 2.** Pearson correlation coefficient (Corr. Coef.) and statistical significance (*p*-value) between observed sea-level data and gulf stream flow for the period between 2006 and 2018.

	Daily Moving avg. (Corr. Coeff., <i>p</i> -Value)	Weekly Moving avg. (Corr. Coeff., <i>p</i> -Value)	Biweekly Moving avg. (Corr. Coeff., <i>p</i> -Value)	Monthly Moving avg. (Corr. Coeff., <i>p</i> -Value)	Quarterly Moving avg. (Corr. Coeff., <i>p</i> -Value)	Semiannual Moving avg. (Corr. Coeff., <i>p</i> -Value)	Annual Moving avg. (Corr. Coeff., <i>p</i> -Value)
No Lag	−0.186, 0.0	−0.222, 0.0	−0.257, 0.0	−0.332, 0.0	−0.368, 0.0	−0.316, 0.0	−0.055, 0.006
7 days Lag	−0.216, 0.0	−0.27, 0.0	−0.337, 0.0	−0.427, 0.0	−0.444, 0.0	−0.371, 0.0	−0.076, 0.0
14 days Lag	−0.295, 0.0	−0.386, 0.0	−0.448, 0.0	−0.507, 0.0	−0.508, 0.0	−0.42, 0.0	−0.093, 0.0
21 days Lag	−0.403, 0.0	−0.484, 0.0	−0.514, 0.0	−0.551, 0.0	−0.555, 0.0	−0.459, 0.0	−0.104, 0.0
30 days Lag	−0.299, 0.0	−0.389, 0.0	−0.464, 0.0	−0.539, 0.0	−0.584, 0.0	−0.493, 0.0	−0.106, 0.0

In Figure 14, a similar comparison is shown between the modeled nontidal forcings and the GS flow. However, the modeled residuals demonstrate a weaker correlation with the GS flow compared to the observed data. Whereas the modeled sea-level variations exhibit an inverse correlation on short time scales, this inverse correlation disappears on longer time scales, unlike the observed data. This discrepancy could be attributed to the fact that the model did not incorporate the GS current. It becomes evident from these comparisons that the GS flow directly impacts the low-frequency sea-level oscillations, and incorporating the GS current into the model is necessary to reduce the water level discrepancy between the simulated and observed values. By incorporating GS effects into the model, a more accurate representation of the water level variations can be achieved in the model simulations.

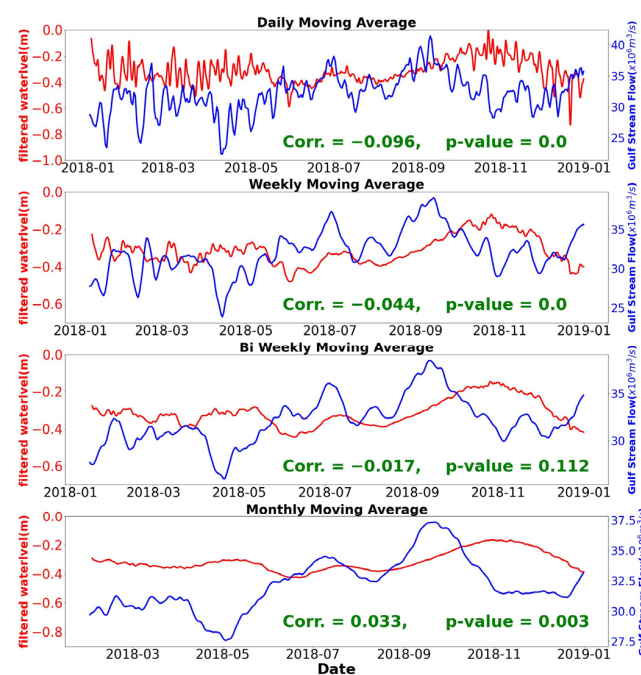


**Figure 14.** Time series of modeled filtered-water level (left axis) at the north jetty and Florida current transport data (right axis) on different time scales: daily (1st panel from top), weekly (2nd panel), biweekly

(3rd panel), and monthly (bottom panel) moving averages. Moving averages for each respective time scale are calculated for both GS flow and filtered-water level.

#### 4.3. Modified Boundary Conditions

The HYCOM data lacks adequate representation of GS flow effects and falls short in effectively simulating low-frequency sea-level oscillations. Consequently, there is a necessity for improved boundary conditions that can effectively consider the influence of GS flow on low-frequency water level variations. To address this, new model boundary conditions are formulated by integrating HYCOM tide data with coastal water level observations filtered to isolate the lower frequency nontidal coastal sea-level record, which is largely driven by GS flow variations as described under Section 1. Nontidal forcings are specifically incorporated into the east boundary nodes (East1A, East2A, East3A, East4A, East5A, and East6A), while HYCOM data for cross-boundaries (North1A, North2A, South1A, South2A, and South3A) are retained without modification as they are distant from GS flow. Figure 15 illustrates this process with an example focusing on the East1A boundary nodes. Figure 15a depicts the tide (blue line) extracted from the HYCOM data at the East1A boundary node, alongside observed low-frequency variations (red line). Figure 15b displays the resulting time series generated by combining the tide and low-frequency variations.

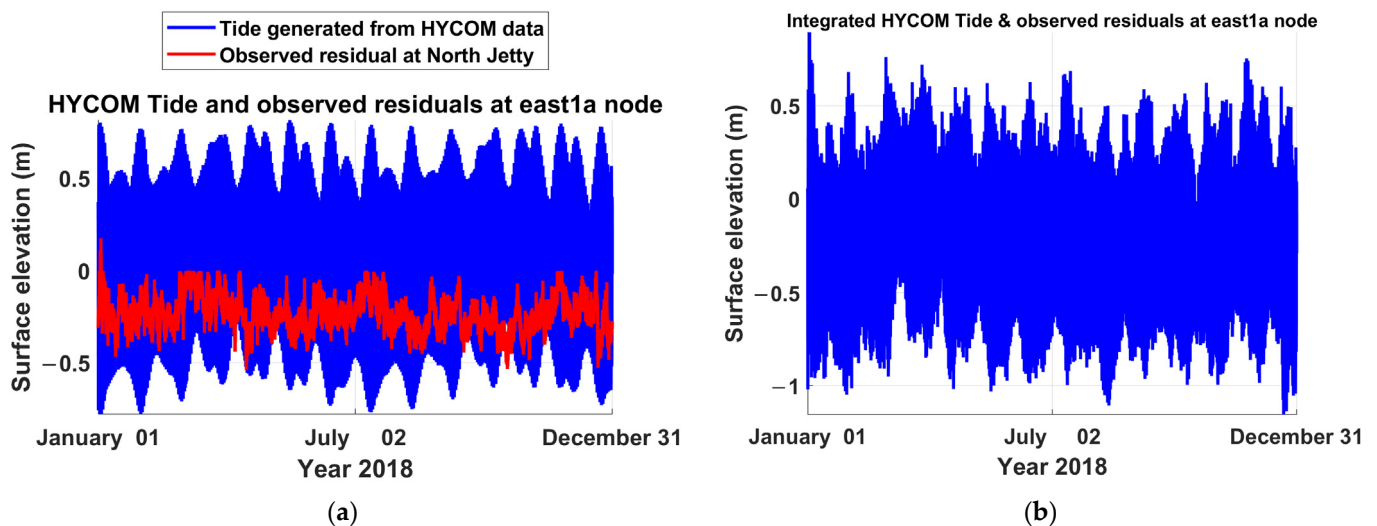


**Figure 15.** New boundary forcings: (a) tide (blue line) derived from HYCOM, and low frequency sea-level variations (red line) derived from measured data at North Jetty station for the East1A boundary node; (b) new flow boundary forcings of surface elevation data at East1A boundary node.

#### 4.4. Model Performance with Modified Boundary Conitions

Delft3D flow model is run with these updated boundary conditions to evaluate whether it demonstrates improvement in simulating low-frequency variations. The simulation results reveal a significant enhancement in capturing low-frequency variation, resulting in a substantial reduction in disparities between observed and modeled data (Figure 16a) and improvement in correlation coefficient by 2% from 0.96 in previous simulation to 0.98 in new simulation (Figure 16b). The bottom panel in Figure 16a illustrates the water level differences between observed and modeled results using both the newly created boundary forcings (red dots) and the old boundary forcings derived from HYCOM surface elevations (blue dots). It is evident that the water level differences between observed and modeled data are reduced by the use of the newly created boundary forcings. Specifically, for the newly created boundary conditions (blue dots), which combine HYCOM tide with observed residuals, the difference ranges from  $-0.1$  to  $0.1$  m (Figure 16a). In contrast, the difference ranges from  $-0.5$  to  $0.5$  m (Figure 10a) for the old boundary conditions based solely on HYCOM surface elevation data.

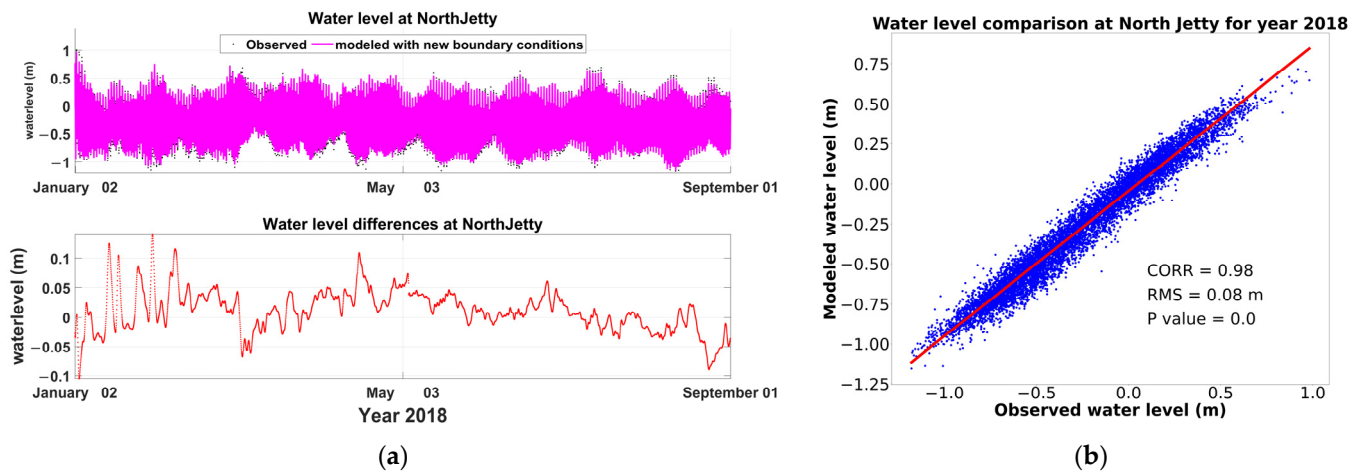


**Figure 16.** Performance of new model simulation: (a) simulated (magenta colored line) and measured (black dots) water level at North Jetty station (**top panel**), differences between modeled and observed data (**bottom panel**); (b) scatter plot for water levels for observed and modeled data at North Jetty for year 2018.

The modeled sea-level oscillations (black line) in Figure 17a exhibit a close match with the observed data (red line). Notably, these simulated results with the newly created boundary conditions demonstrate a substantial reduction in discrepancies with the observed data, as compared to the results from previous simulations (blue line). The differences between modeled and observed sea-level oscillations are drastically reduced for the new boundary conditions, as illustrated in the bottom panel of Figure 17b. Whereas the differences range from  $-0.4$  to  $0.2$  m for the old boundary conditions, they reduce to  $-0.1$  m to  $0.1$  m, often approaching 0, for the new boundary conditions. The significant reduction in this difference underscores the effectiveness of the newly created boundary conditions, incorporating HYCOM tide and observed residuals, in improving the model’s accuracy in simulating sea-level variations.

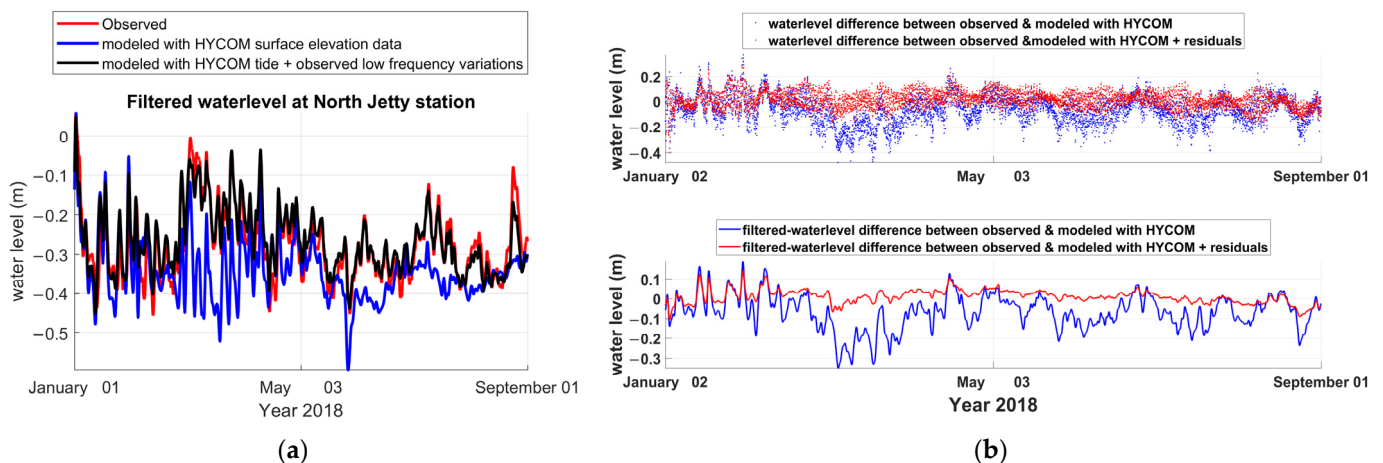


**Figure 17.** Performance of new model simulation: (a) low-frequency sea-level oscillation of observed (red line), modeled with HYCOM surface elevation data (blue line), and modeled with HYCOM tide plus observed low-frequency sea-level variations (black line) at North Jetty station; (b) (**top panel**) illustrates water level differences between measured and simulated with new boundary conditions (red dots) and the water level differences between measured and simulated with old boundary conditions (blue dots). The (**bottom panel**) presents a similar plot for filtered water level differences.

In Figure 18, a comparison is made between the newly modeled sea-level oscillations and the GS flow across various time scales: daily, weekly, biweekly, and monthly. Notably,

the modeled water level demonstrates a better correlation with the GS flow compared to the previous model run utilizing solely HYCOM data. In shorter time scales, the modeled sea-level variations exhibit an inverse correlation, like previous simulations. However, unlike before, this inverse correlation persists even on longer time scales. Moreover, the correlation between the GS and modeled sea-level oscillation closely resembles that of the observed data and GS. Whereas a small difference remains between modeled and observed sea-level data, the modeled sea-level with new boundary conditions shows a significant improvement compared to previous simulations. This suggests a notable improvement in the model’s ability to accurately represent sea-level oscillation.

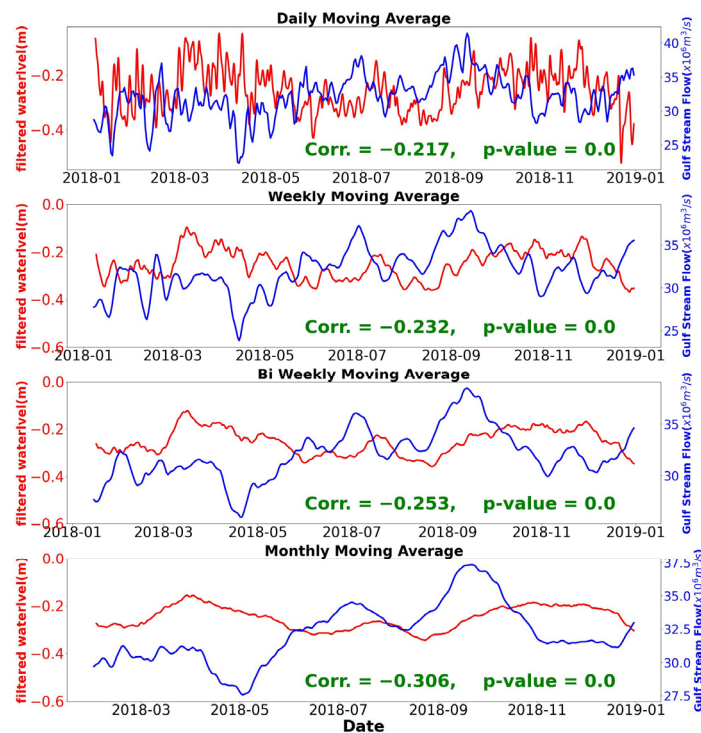


**Figure 18.** Filtered-water level (left axis) for new simulation at North Jetty and Florida current transport data (right axis) on various time scales: daily (1st panel from top), weekly (2nd panel), biweekly (3rd panel), and monthly (bottom panel) moving averages. Moving averages for each respective time scale are calculated for both GS flow and filtered-water level.

### 5. Discussion and Conclusions

A high resolution coastal and estuarine model had been constructed utilizing Delft3D for central IRL, Florida, to reproduce hydrodynamic processes and transport phenomena. Here it was considered sea surface elevation, comprising tides and nontidal forcings, meteorological forcings, and transport boundary forcings. In assessing its performance, modeled results, such as water level, salinity, water temperature, and currents, were evaluated against the observed data. In general, the modeled results closely matched the observations, particularly regarding the key parameters.

The comparison of water levels between the simulated and observations at North Jetty station demonstrates a strong correspondence between the modeled water levels and the observations with a coefficient of determination equal to 0.96 (Figure 10). However, noticeable discrepancies between the two datasets are evident. The differences between the simulated and observed tide is significantly smaller than the differences in water levels (Figure 11), indicating that nontidal forcings play a more significant role in the differences observed. When comparing simulated and observed low-frequency variations, significant differences were observed, especially when contrasted with the disparities between the simulated and HYCOM’s low-frequency variations (Figure 12). It implies the accuracy of

the simulation outputs is closely tied to the quality of HYCOM sea surface elevation data used as boundary forcings. Furthermore, it indicates that the HYCOM data inadequately represent the GS effects on sea-level oscillation. Consequently, the disparity between the water levels may stem from the inadequate incorporation of the GS effects in HYCOM sea surface elevation data.

Figure 13 present a comparison between the observed sea-level oscillations at the North Jetty station and the GS flow across various time scales (daily, weekly, biweekly, monthly, quarterly, semiannual, and annual) using moving averages. A strong correlation between nontidal forcings in the water level and the GS flow emerges (Table 2), particularly at longer time scales, illustrating the significant influence of the GS on water level variations. However, Figure 14 reveals a weaker correlation between the modeled sea-level variations and the GS flow, due to the model's lack of incorporation of the GS current.

This study addresses the limitations of HYCOM data in adequately representing GS flow effects and low frequency sea-level oscillations, necessitating improved boundary conditions. New flow boundary conditions were formulated (Figure 15) by integrating HYCOM tide data and observed nontidal forcings, specifically focusing on the east boundary nodes. Subsequently, the Delft3D flow model was run with these updated boundary conditions, resulting in a significant enhancement in simulating low-frequency variations and reducing disparities between observed and modeled data (Figures 16 and 17). The modeled sea-level oscillations closely match the observed data, indicating substantial improvement compared to previous simulations with the HYCOM data. Figure 18 illustrates a comparison between modeled sea-level oscillations and GS flow, highlighting the improved correlation across various time scales and the model's enhanced accuracy in representing sea-level variations.

These findings suggest that the flow of the GS directly influences low frequency sea-level variations and integrating the GS effects into the model can enhance the accuracy of water level simulations and reduce discrepancies with observations. However, a problem may arise in implementing this approach in a real-time forecasting system. Predictions for nontidal forcings are essential, but they are unavailable for the forecast period. Machine learning (ML) techniques may offer a solution to this challenge. A machine learning model can be constructed by training and testing it with observed nontidal forcing data. Subsequently, the performance of ML can be evaluated by testing it with a simulation run and subsequently assessing the simulation results against measured data. Upon achieving satisfactory results, the ML can be employed to forecast low-frequency data. These forecasted low-frequency data can then be combined with HYCOM tide data to generate flow boundary conditions.

**Author Contributions:** Conceptualization, G.A.Z. and M.A.H.; methodology, M.A.H.; software, M.A.H.; validation, G.A.Z.; formal analysis, M.A.H.; investigation, M.A.H.; resources, G.A.Z.; data curation, M.A.H.; writing—original draft preparation, M.A.H.; writing—review and editing, G.A.Z. and M.A.H.; visualization, M.A.H.; supervision, G.A.Z.; project administration, G.A.Z. All authors have read and agreed to the published version of the manuscript.

**Funding:** This study has been supported by the Sebastian Inlet Tax District and Florida Institute of Technology.

**Institutional Review Board Statement:** Not applicable.

**Informed Consent Statement:** Not applicable.

**Data Availability Statement:** All data, model results, and programming scripts could be found at the following link: [https://drive.google.com/drive/u/0/folders/1-9FBjwJWFy1TvBuuk\\_9ZNM654pNzPuaS](https://drive.google.com/drive/u/0/folders/1-9FBjwJWFy1TvBuuk_9ZNM654pNzPuaS) (created on 20 February 2024).

**Acknowledgments:** The authors would like to thank the Sebastian Inlet Tax District for supporting this research and the reviewers for their insightful comments.

**Conflicts of Interest:** The authors declare no conflicts of interest.

## References

1. Auclair, F.; Estournel, C.; Marsaleix, P.; Pairaud, I. On coastal ocean embedded modeling. *Geophys. Res. Lett.* **2006**, *33*, 14. [CrossRef]
2. Beckers, J.M.; Brasseur, P.; Nihoul, J. Circulation of the western mediterranean: From global to regional scales. *Deep Sea Res. Part II Top. Stud. Oceanogr.* **1997**, *44*, 531–549. [CrossRef]
3. Cailleau, S.; Fedorenko, V.; Barnier, B.; Blayo, E.; Debreu, L. Comparison of different numerical methods used to handle the open boundary of a regional ocean circulation model of the Bay of Biscay. *Ocean Model.* **2008**, *25*, 1–16. [CrossRef]
4. Penven, P.; Debreu, L.; Marchesiello, P.; McWilliams, J.C. Evaluation and application of the ROMS 1-way embedding procedure to the central California upwelling system. *Ocean Model.* **2006**, *12*, 157–187. [CrossRef]
5. Tomczak, M. *Shelf and Coastal Oceanography*; University of Maine: Orono, ME, USA, 1998.
6. Ezer, T.; Atkinson, L.P.; Corlett, W.B.; Blanco, J.L. Gulf Stream's induced sea-level rise and variability along the us mid-Atlantic coast. *J. Geophys. Res. Ocean* **2013**, *118*, 685–697. [CrossRef]
7. Ezer, T. The long-term and far-reaching impact of hurricane Dorian (2019) on the Gulf Stream and the coast. *J. Mar. Syst.* **2020**, *208*, 103370. [CrossRef]
8. Habib, M.A.; Zarillo, Z.A. Construction of a Real-Time Forecast Model for Coastal Engineering and Processes Nested in a Basin Scale Model. *J. Mar. Sci. Eng.* **2023**, *11*, 1263. [CrossRef]
9. NOAA Scijinks. Available online: <https://scijinks.gov/gulf-stream/> (accessed on 27 April 2024).
10. Google Earth Version 9.185.0.0. Sebastian, Florida, USA. Available online: <https://earth.google.com/> (accessed on 21 March 2023).
11. Deltares, D. *Simulation of Multi-Dimensional Hydrodynamic Flows and Transport Phenomena, Including Sediments*; Version 4.05; Delft3D-Flow User Manual: Delft, The Netherlands, 2022. Available online: <https://oss.deltares.nl/web/delft3d/manuals> (accessed on 16 February 2023).
12. Smith, N.P. Tidal and nontidal flushing of Florida's Indian River Lagoon. *Estuaries* **1993**, *16*, 739–746. [CrossRef]
13. Smith, N.P. Seasonal-scale transport patterns in a multi-inlet coastal lagoon. *Estuar. Coast. Shelf Sci.* **2001**, *52*, 15–28. [CrossRef]
14. NOAA National Geophysical Data Center. *1/3 Arc-Second MHW Coastal Digital Elevation Model*; NOAA National Centers for Environmental Information: Palm Beach, FL, USA, 2010. Available online: <https://www.ncei.noaa.gov/access/metadata/landing-page/bin/iso?id=gov.noaa.ngdc.mgg.dem:427> (accessed on 13 November 2021).
15. Metzger, E.J.; Helber, R.W.; Hogan, P.J.; Posey, P.G.; Thoppil, P.G.; Townsend, T.L.; Wallcraft, A.J.; Smedstad, O.M.; Franklin, D.S.; Zamudio, L.; et al. *Global Ocean Forecast System 3.1 Validation Testing*. NRL Report; Naval Research Lab Stennis Detachment: Stennis Space Center, MS, USA, 2017; NRL/MR/7320-17-9722. Available online: <https://hycom.org> (accessed on 19 April 2022).
16. Mesinger, F.; DiMego, G.; Kalnay, E.; Mitchell, K.; Shafran, P.C.; Ebisuzaki, W.; Jović, D.; Woollen, J.; Rogers, E.; Berbery, E.H.; et al. North American Regional Reanalysis: A long-term, consistent, high-resolution climate dataset for the North American domain, as a major improvement upon the earlier global reanalysis datasets in both resolution and accuracy. *Bull. Am. Meteorol. Soc.* **2006**, *87*, 343–360. [CrossRef]
17. St. Johns River Water Management District (SJRWMD) Hydrologic Data. Available online: <https://www.sjrwmd.com/data/> (accessed on 20 March 2019).
18. Leendertse, J.J. *Aspects of a Computational Model for Long-Period Water-Wave Propagation*; RAND Corp.: Santa Monica, CA, USA, 1967.
19. Leendertse, J.J.; Gritton, E.C. *A Water-Quality Simulation Model for Well Mixed Estuaries and Coastal Seas: Volume II: Computation Procedures*; RAND Corp.: Santa Monica, CA, USA, 1971; p. 53.
20. Leendertse, J.J.; Alexander, R.C.; Liu, S.K. *A Three-Dimensional Model for Estuaries and Coastal Seas: Volume I, Principles of Computation*; RAND Corp.: Santa Monica, CA, USA, 1973.
21. Octavio, K.A.H.; Jirka, G.H.; Harleman, D.R.F. Vertical Heat Transport Mechanisms in Lakes and Reservoirs. Ph.D. Thesis, Massachusetts Institute of Technology, Cambridge, MA, USA, 1977.
22. Harbor Branch Oceanographic Institute's (HBOI) Land/Ocean Biogeochemical Observation (LOBO) Stations. Available online: <http://fau-hboi.loboviz.com/loboviz/> (accessed on 25 February 2020).
23. The Costal Process Research Group at Florida Tech. Available online: <https://research.fit.edu/wave-data/real-time-data/> (accessed on 7 June 2020).
24. Pawlowicz, R.; Beardsley, B.; Lentz, S. Classical tidal harmonic analysis including error estimates in MATLAB using T\_TIDE. *Comput. Geosci.* **2002**, *28*, 929–937. [CrossRef]
25. NOAA. Florida Current Transport Time Series and Cruises. Available online: [www.aoml.noaa.gov/phod/floridacurrent](http://www.aoml.noaa.gov/phod/floridacurrent) (accessed on 14 December 2023).

**Disclaimer/Publisher's Note:** The statements, opinions and data contained in all publications are solely those of the individual author(s) and contributor(s) and not of MDPI and/or the editor(s). MDPI and/or the editor(s) disclaim responsibility for any injury to people or property resulting from any ideas, methods, instructions or products referred to in the content.